A Controlled Ex Situ Experiment for Exploring the Biological Sources of Variability in Microbially Induced Sedimentary Structures (MISS) Formation

Liza Alexandra Fernandez, Dov Corenblit, Florent Arrignon, Stéphanie Boulêtreau, Neil S. Davies, Jessica Ferriol, Frédéric Julien, Joséphine Leflaive, Thierry Otto, Erwan Roussel, et al.

AbSciCon

Providence, Rhode Island, USA
5–10 May 2024

A Controlled Ex Situ Experiment for Exploring the Biological Sources of Variability in Microbially Induced Sedimentary Structures (MISS) Formation

Liza Alexandra Fernandez

Dov Corenblit, Florent Arrignon, Stéphanie Boulêtreau, Neil S. Davies, Jessica Ferriol, Frédéric Julien, Joséphine Leflaive, Thierry Otto, Erwan Roussel, Johannes Steiger, Jean-Pierre Toumazet

Context

Extraterrestrial Life ?

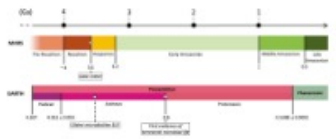

Timeline of Earth (Cohen et al., 2013) and Mars (Kite, 2019; Rapin et al., 2023) periods

With the latest developments of orbital measurement technologies and instruments, such as satellites, as well as surface instruments, such

OPEN

Material & Methods

MISS type

There are a multitude of forms of MISS (Davies et al., 2016; Gerdes, 2007; Noffke, 2010; Noffke et al., 2001b; Schieber et al., 2007). For this study, we have chosen to focus on mat cracks, which are present in the fossil and modern record (Noffke, 2010). This type of structure is also of interest in terms of the limits of the distinction between biotic and abiotic structures, which in this case are desiccation cracks in terms of their abiotic equivalent (Corenblit et al., 2023; Davies et al., 2016). Mat cracks result from the activity of a biofilm, or microbial mat, colonizing a surface in damp muddy siliciclastic depositional systems.

OPEN

Results & Discussion

Ex situ observations

From the dried results of experiments carried out at the CRBE laboratory in Toulouse, we have obtained mat cracks.

Observation levels

There are a first sandy topographic level (bottom) and a second clay topographic level (top) with (C, D, G and M) or without (A) the presence of a biofilm on the latter. A network of primary cracks is observed, corresponding to the widest separations between the clay parts, where the sandy matrix below can be seen. Networks of secondary cracks are visible on the sandy (parallel to the primary cracks) and clayey (not parallel

OPEN

Conclusions/Perspectives

Under controlled conditions, the laboratory experiment highlighted the variability between abiotic and biotic treatments, as well as within biotic treatments themselves, with or without different biomass scales. These initial observations showed that diatoms can be distinguished from other biotic treatments. What's more, the geomorphological modifications induced by the presence of biofilms are clearly visible to the naked eye when comparing abiotic controls.

Statistical analysis revealed trends in inter- and intra-group variability. Abiotic structures were clearly different, confirming initial observations. Diatoms again showed different relief trends, with

OPEN

Objectives

The aim of this research is to develop a new technique for the automatic detection of biotic signatures on modern and ancient sedimentary surfaces in the case study of MISS, focusing on mat cracks. This method is based on :

(i) a better understanding of mat crack type MISS thanks to laboratory observations under controlled conditions and field observation in recent and fossil records;

(ii) the constitution of a database of images representing MISS and their abiotic equivalents;

(iii) to couple AI with a classical statistical study to

OPEN

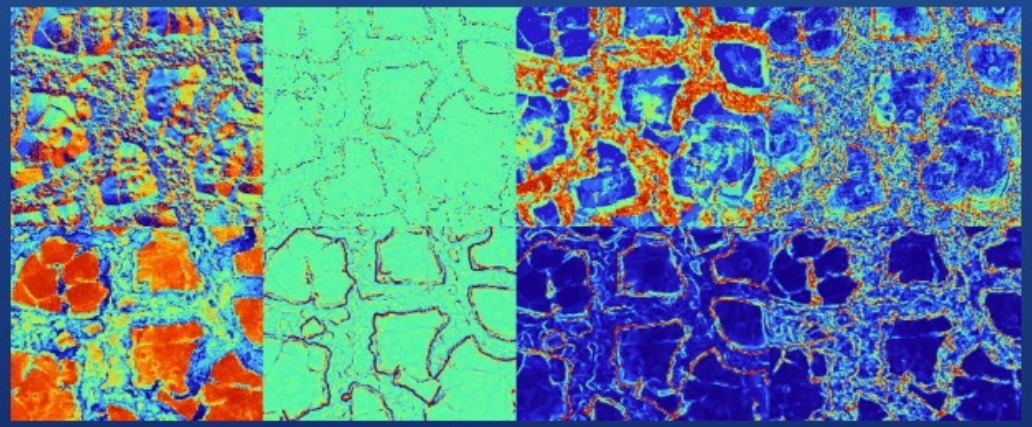

Acknowledgements

This work is a collaboration between several universities: the Université de Clermont Auvergne (Clermont-Ferrand, France), the Université Toulouse III - Paul Sabatier (Toulouse, France) and the University of Cambridge (Cambridge, UK). This research work is carried out in several French laboratories: Laboratoire de Géographie Physique et Environnementale (GEOLAB, UMR 6042, Clermont-Ferrand), Centre de Recherche sur la Biodiversité et l'Environnement (CRBE, UMR 5300, Toulouse) and the Geosciences Environnement Toulouse laboratory (GET, UMR 5563, Toulouse). AI development is in collaboration

OPEN

ABSTRACT

A Controlled Ex Situ Experiment for Exploring the Biological Sources of Variability in Microbially Induced Sedimentary Structures (MISS) Formation

Liza Alexandra Fernandez[1,2], Dov Corenblit[2], Florent Arrignon[3], Stéphanie Bouletreau[2], Neil S. Davies[4], Jessica Ferriol[2], Frédéric Julien[2], Joséphine Leflaive[2], Thierry Otto[2], Erwan Roussel[1], Johannes Steiger[1], and Jean-Pierre Toumazet[1]

[1]Université Clermont Auvergne, CNRS, GEOLAB, Clermont-Ferrand, France.

[2]Université Toulouse III – Paul Sabatier, CNRS, CRBE, Toulouse, France.

[3]MAD-Environnement, Nailloux, France.

[4]Department of Earth Sciences, University of Cambridge, Cambridge, United Kingdom

Mars, with its physicochemical conditions resembling Earth's environment 4.5 to 3.5 Ga ago, is a planet of interest in the search for past conditions adequate to life (Cabrol, 2018; Mangold et al., 2021). Sedimentary rocks, specifically their geomorphological properties, have been identified as a promising avenue for detecting bacterial activity in ancient Martian environments (Noffke, 2021).

Most particularly, Microbially Induced Sedimentary Structures (MISS), well-preserved on Earth in rocks dating back millions of years, raise the possibility of identifying similar structures on Mars (Noffke, 2015). The use of expert knowledge for the search of MISS on Mars is based on abductive inference, assuming that similar physicochemical processes should lead to sedimentary morphologies with similar characteristics as on Earth (Corenblit et al., 2019).

Observations, like mud cracks in Gale Crater, by the Curiosity rover, confirm environmental conditions suitable for MISS formation on Mars surface 3.8 Ga (Rapin et al., 2023). It was suggested that the use of geomorphological visual descriptors in images captured by Martian rovers to identify MISS in rocks may be conclusive (Corenblit et al., 2023). However, validating the biotic origin of MISS-like structures remains challenging, since purely abiotic, i.e., physicochemical processes can produce structures resembling those left by fossilized microbial mats (Davies et al., 2016). Visual expertise thus requires a detailed and robust understanding of morphological parameters specific to MISS.

Until now, research efforts mostly focused on distinguishing signatures in rocks of purely abiotic origin from those with a biotic origin, with the primary concern being the avoidance of false positives in MISS identification (Davies et al., 2016). The variability of morphological signatures in sediments in relation to microbial mat type and biomass (i.e., biological sources of variability in sedimentary rocks) has not yet been thoroughly explored. The form(s) Martian life might have taken and its abundance in ancient sedimentary environments remain uncertain. Here, we are exploring the hypothesis that microorganism consortia in shallow waters have given rise to various types of MISS due to potential variations in the quality and abundance of microbial mats.

To address the question of biological sources of variability in morphological aspects of sedimentary rocks, a controlled experiment was conducted at the Laboratory of Functional Ecology and Environment in Toulouse (now: CRBE), France. The objective was to investigate the development of microbial mats on an immersed sedimentary surface, along with the resulting desiccation cracks, and to examine their morphological characteristics. The experiment involved both the absence and presence of different types of microbial mats (including cyanobacteria, diatom, green algae and a mixture of the three types), each with two levels of biomass. This laboratory study was conducted in a phytotron and greenhouse with the aim to assess in controlled conditions the inter- and intragroup variability in the morphological response of a specific substrate composed of layers of sand and clay to the presence of different microbial mats. The study encompassed conditions both without (abiotic control) and with the four microbial mat treatments.

Beyond distinguishing abiotic and biotic situations, the experiment delineated geomorphological variability from biological variability in MISS formation. Analyses, supported by statistical tools and convolutional neural networks (CNN), permitted to identify 2D and 3D discriminative parameters and resolution scales between controls and treatments and among different biotic treatments. This research provides new insights into the potential of automatic detection of ancient Martian biosignatures visible in rover images.

CONTEXT

Extraterrestrial Life ?

With the latest developments of orbital measurement technologies and instruments, such as satellites, as well as surface instruments, such as rovers employed on Mars, the research for potential traces of extraterrestrial life is burgeoning. Thanks to NASA's Curiosity and Perseverance rovers and their camera equipment (e.g., ChemCam and SuperCam), it is possible to propose a new perspective for the detection of potential life signatures on Mars based on the analysis of geochemical and geomorphological variables in sedimentary surfaces. The research for fossil or modern signatures of life on the surface of telluric planets and their satellites can be based on the detection of fossilized microorganisms, biologically influenced minerals and chemical or isotopic biomarkers (Greaves et al., 2021; Westall et al., 2015). Given the similarities in initial conditions between Earth and Mars, there is a strong presumption that if microorganisms evolved on Mars during the Noachian period (>3.6 Ga), in habitats such as crater lakes, they affected these geomorphological features at their surface (Noffke and Awramik, 2013; Westall et al., 2021). Also, in the contrary to Earth, crust recycling, which makes it difficult to study ancient surfaces, between 3.5 and 4 Ga or even more, is absent on Mars (Lapôtre et al., 2022). Consequently, absence of crust recycling on Mars represents an advantage to the search for potential ancient biosignatures on its surface. An example of a potentially interesting environment for the development of microorganisms was shown recently at Gale crater surface, where polygonal mud (or desiccation) cracks, characteristic of a sustained wet-dry cycling, were described (Rapin et al., 2023).

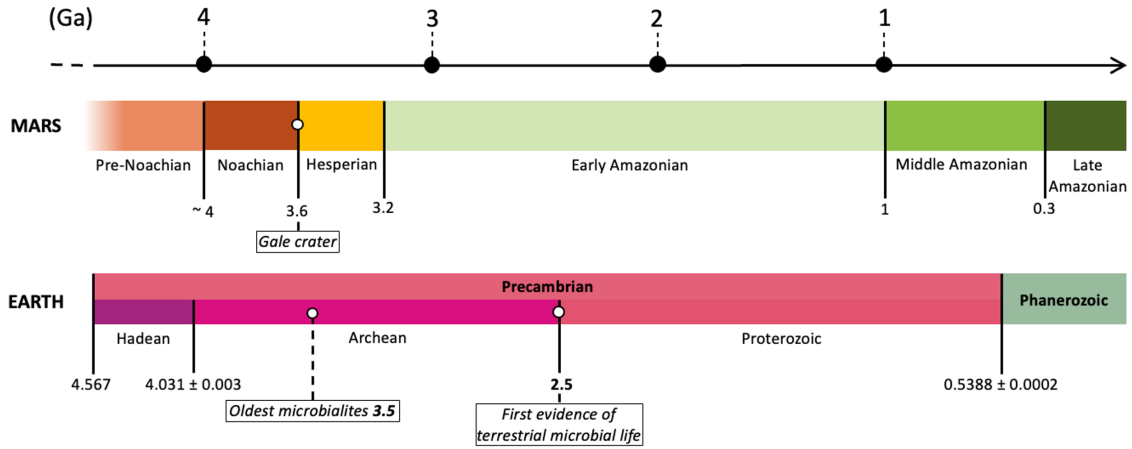

Timeline of Earth (Cohen et al., 2013) and Mars (Kite, 2019; Rapin et al., 2023) periods

Potential signatures

Among the candidates for potential biosignatures, sediments that may have been influenced by microbial activity were proposed by (Noffke, 2010). These candidates identified in ancient rocks (e.g., Ordovician and Permian rocks in the Montagne Noire, France) are called "MISS", Microbially Induced Sedimentary Structures (Noffke et al., 1996) and were proposed as analogous models relevant to the search for signatures of life on Mars (Noffke, 2021, 2015, 2010).

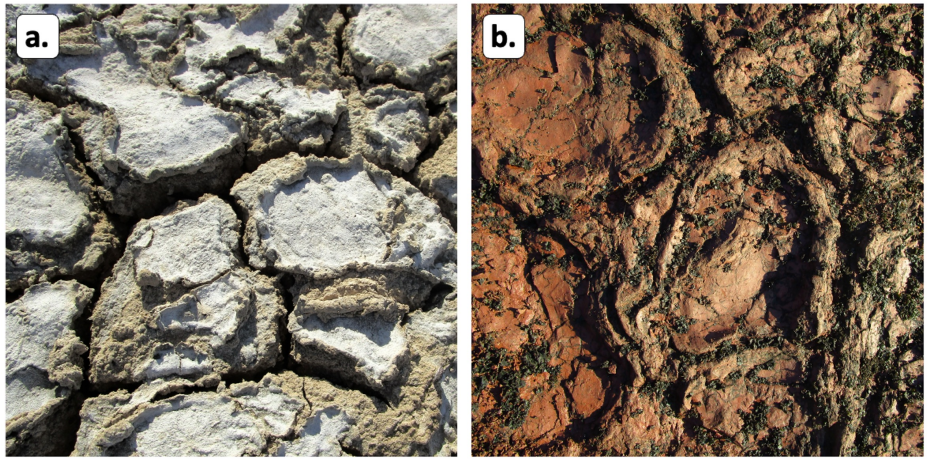

Microbially Induced Sedimentary Structures a. modern (Peyriac-de-Mer, France), b. Permian fossil (Salagou, France)

CONTEXT

Noffke et al. (2001a) defined MISS as a new category within the classification of primary sedimentary structures (Pettijohn and Potter, 1964), this is: “bedding modified by microbial mats or biofilms”. These structures form at water/sediment interfaces and can take many forms depending on the metabolism of the microorganisms present and the sediment dynamics of the environment (Gerdes, 2007; Noffke, 2010; Schieber et al., 2007). The wealth of data on MISS from Earth is possible for their presence in the modern (Bose and Chafetz, 2009; Gerdes et al., 2000; Noffke, 1998; Noffke et al., 2003; Schieber et al., 2007) and fossil record (Davies et al., 2016, 2017; Noffke et al., 2001a; Noffke, 2008; Noffke et al., 2008; Pruss et al., 2004). The interest of MISS in the search for signatures of ancient life on Earth and on Mars can be supported with the first evidence of terrestrial microbial life dated at 2.5 Ga (Viles, 2012). Also, microbialites, i.e. sedimentary structures formed by microbial influence such as stromatolites especially in vertical section, and MISS also present in bedding planes (Noffke and Awramik, 2013), are dated to 3.5 Ga on Earth (Awramik, 2006; Awramik and Grey, 2005; Hofmann et al., 1999).

A New Approach

Expert knowledge of biogenic geomorphological structures (e.g., MISS), from micro (inframillimeter to centimeter) to meso (centimeter to decameter) spatial scales, for which the biotic origin is well recognized, or at least strong clues exist, can be employed to search for potential signatures of life on Mars (Cady et al., 2003; Noffke, 2010). Such a method is based on reasoning by abductive inference with the assumption that identical, or equivalent, (bio)geomorphological processes produce similar (bio)geomorphological structures. Using the Earth as a geological analogue for Mars, we hypothesize that potential microbial life on Mars could have given rise, on the planet’s surface, to a variety of recognizable types of biogenic geomorphological structures, such as MISS (Corenblit et al., 2019). This novel approach requires the development of a conceptual and methodological framework specifically adapted to the distinction of abiotic and biotic sedimentary structures (Corenblit et al., 2023; Davies et al., 2016). In the case that biotic structures are detected, the variability of their morphological aspects must be considered.

Expert knowledge of biogenic geomorphological structures (e.g., MISS), from micro (inframillimeter to centimeter) to meso (centimeter to decameter) spatial scales, for which the biotic origin is well recognized, or at least strong clues exist, can be employed to search for potential signatures of life on Mars (Cady et al., 2003; Noffke, 2010). Such a method is based on reasoning by abductive inference with the assumption that identical, or equivalent, (bio)geomorphological processes produce similar (bio)geomorphological structures. Using the Earth as a geological analogue for Mars, we hypothesize that potential microbial life on Mars could have given rise, on the planet’s surface, to a variety of recognizable types of biogenic geomorphological structures, such as MISS (Corenblit et al., 2019). This novel approach requires the development of a conceptual and methodological framework specifically adapted to the distinction of abiotic and biotic sedimentary structures (Corenblit et al., 2023; Davies et al., 2016). In the case that biotic structures are detected, the variability of their morphological aspects must be considered.

In-depth statistical analyses of these images enabled us to identify and extract key variables, in 2D and 3D, of biotic and abiotic forms (texture, shape, pattern). In a second step, using artificial intelligence, i.e., a supervised deep learning procedures based on convolutional neural networks (CNN) architecture, this data will then be used for the development of a model that shall permit to distinguish between biotic (MISS) and abiotic (equivalent geological context such as desiccation cracks) structures. The main development stages using artificial intelligence will be: (i) image pre-processing (normalization, augmentation) to homogenize and increase the robustness of images data; (ii) the development of a classifier based on CNN using RGB images ; (iii) the exploration of effects of 3D data inclusion and the visualization of Region of Interests using Class Activation Maps. Objective image classification can potentially lead to the formation of distinct biotic groups in cases where microorganisms significantly affect one or more key parameters.

OBJECTIVES

The aim of this research is to develop a new technique for the automatic detection of biotic signatures on modern and ancient sedimentary surfaces in the case study of MISS, focusing on mat cracks. This method is based on :

(i) a better understanding of mat crack type MISS thanks to laboratory observations under controlled conditions and field observation in recent and fossil records;

(ii) the constitution of a database of images representing MISS and their abiotic equivalents;

(iii) to couple AI with a classical statistical study to identify potential variables constituting a signature of life on the samples observed;

(iv) a recognition of biogenic or non-biogenic structures as well as a classification of potential biosignatures based on convolutional neural networks.

This approach, still confined to terrestrial samples, is intended to be applied to images of the surface of Mars. This future step requires the optimization of the protocol to adapt it to the constraints of Martian research.

MATERIAL & METHODS

MISS type

There are a multitude of forms of MISS (Davies et al., 2016; Gerdes, 2007; Noffke, 2010; Noffke et al., 2001b; Schieber et al., 2007). For this study, we have chosen to focus on mat cracks, which are present in the fossil and modern record (Noffke, 2010). This type of structure is also of interest in terms of the limits of the distinction between biotic and abiotic structures, which in this case are desiccation cracks in terms of their abiotic equivalent (Corenblit et al., 2023; Davies et al., 2016). Mat cracks result from the activity of a biofilm, or microbial mat, colonizing a surface in damp muddy siliciclastic depositional systems.

Mat cracks can easily be seen, for example, at the edges of ponds, lakes, and rivers. A thick elastic membrane binds the sediment. It is also possible to observe a gradient in the formation of the various mat cracks present in the environment, with, for example, the size of their tear opening.

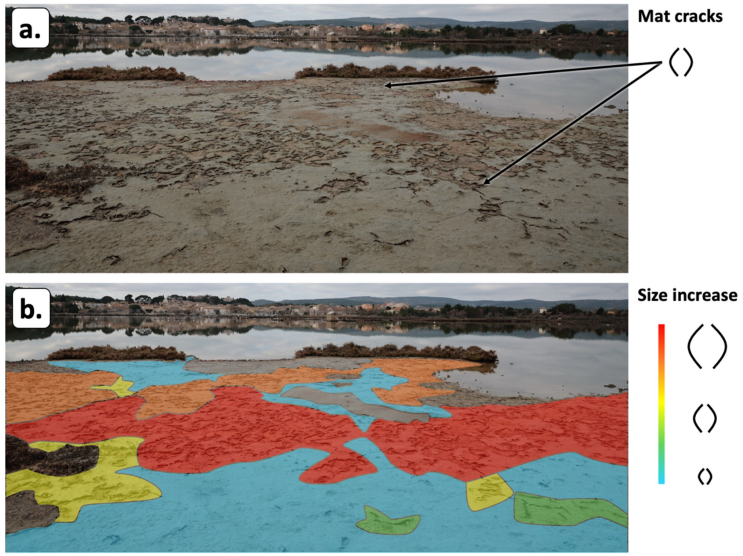

Ponds of Thau (Southern France) a. Mat cracks in environmental context, b. Gradient of mat crack opening sizes in the environment

MATERIAL & METHODS

As the surface dries out, cracks appear until the MISS membrane tears completely. This tear leaves the sedimentary support underneath exposed, which, once the membrane protection has been removed after tearing, will in turn witness the formation of desiccation cracks. These dynamic formation conditions may vary according to environmental conditions, the consortium of microorganisms making up the biofilm or microbial mat, and the sediments.

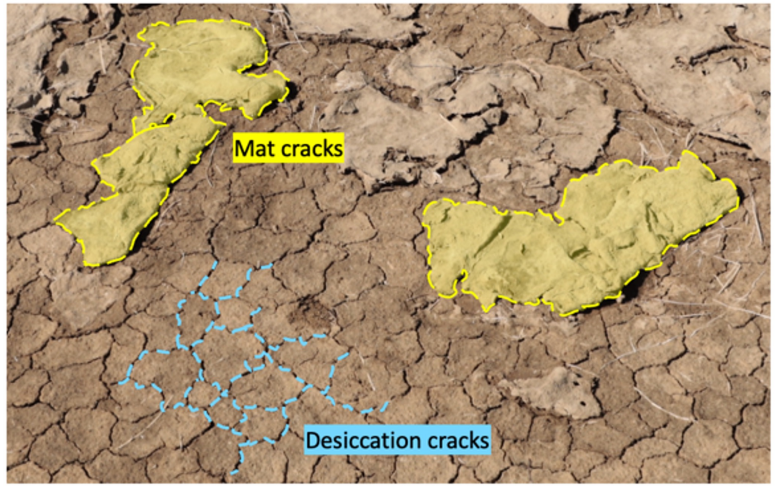

Drying out of mat cracks and formation of desiccation cracks

Ex situ experiment

To explore the variability in the formation of the mat-cracks, we designed an experiment under controlled conditions at the CRBE laboratory in Toulouse, France. The aim was to study the development of biofilms on an immersed surface under drying conditions, and to examine the morphological characteristics of the resulting surface.

Several types of treatment are present in this experiment, all replicated five times, except for the abiotic controls (A) – which have no added microbial strain – replicated ten times, all distributed in open plastic trays of 29*19*7-centimeter. The sediment base is composed of a layer of sand (mass = 1080 g; grain size < 3000 µm) overlaid by a layer of clay (mass = 240 g; grain size < 120 µm). The water used in the experiment is from the Volvic brand, whose composition is well known, with neutral or even slightly alkaline properties. Three microbial strains were tested: cyanobacteria (C), diatoms (D) and green algae (G). An additional treatment was added to the study: mixed (M), which is a mixture of C, D and G representing 3/13, 5/13 and 5/13 of M respectively. These treatments (C, D, G and M) are doubled into two biomasses: low (1) and high (2), with a ratio of 5. The result is 9 different types of treatment: A, C1, C2, D1, D2, G1, G2, M1, M2.

To explore the variability in the formation of the mat-cracks, we designed an experiment under controlled conditions at the CRBE laboratory in Toulouse, France. The aim was to study the development of biofilms on an immersed surface under drying conditions, and to examine the morphological characteristics of the resulting surface.

Several types of treatment are present in this experiment, all replicated five times, except for the abiotic controls (A) – which have no added microbial strain – replicated ten times, all distributed in open plastic trays of 29*19*7-centimeter. The sediment base is composed of a layer of sand (mass = 1080 g; grain size < 3000 µm) overlaid by a layer of clay (mass = 240 g; grain size < 120 µm). The water used in the experiment is from the Volvic brand, whose composition is well known, with neutral or even slightly alkaline properties. Three microbial strains were tested: cyanobacteria (C), diatoms (D) and green algae (G). An additional treatment was added to the study: mixed (M), which is a mixture of C, D and G representing 3/13, 5/13 and 5/13 of M respectively. These treatments (C, D, G and M) are doubled into two biomasses: low (1) and high (2), with a ratio of 5. The result is 9 different types of treatment: A, C1, C2, D1, D2, G1, G2, M1, M2.

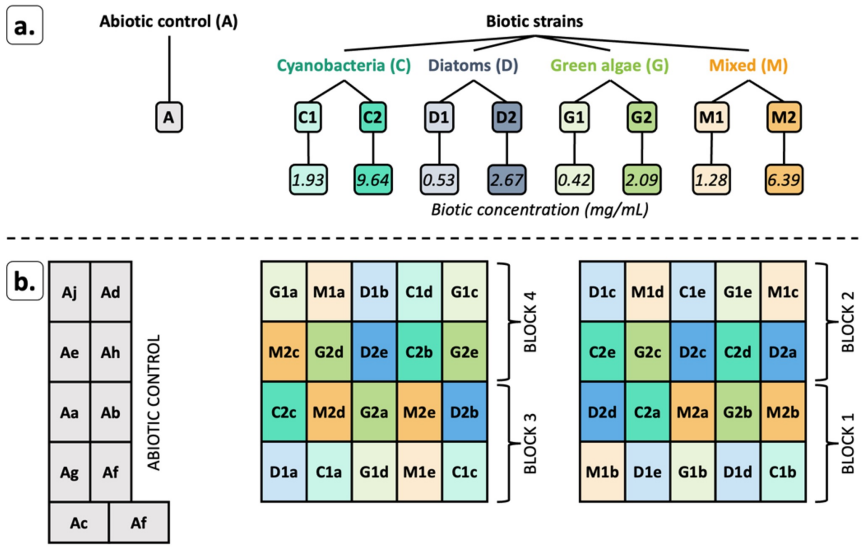

Design of the ex-situ experiment a. Distribution of biotic concentrations between treatment ; b. Distribution plan of tanks in the phytotron

MATERIAL & METHODS

The treatments were all placed in the phytotron for the duration of the biofilm growth period (11 days for low biomass and 21 days for high biomass). At the end of the allotted time, the water in the tanks was siphoned off and the tanks were taken to the greenhouse, where the residual water could finish evaporating. The following analyses are based on fully dried treatments.

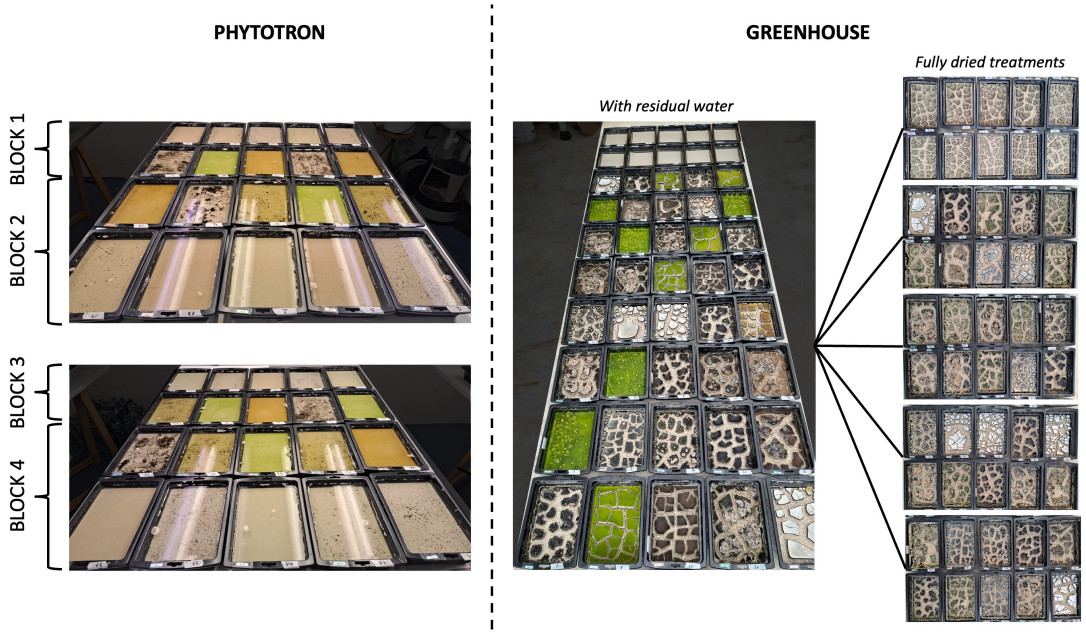

Biotic treatment tanks in the phytotron and drying of treatments in the greenhouse.

In situ observations

The laboratory experiment also represents a field reality.

Microbial studies

The three strains of microorganisms chosen represent a variety of aquatic environments (e.g., oceans, lakes, rivers) where MISS can be found, including mat cracks. Cyanobacteria are photosynthetic bacteria, with some species forming algal blooms under bright, nutrient-enriched conditions. Diatoms are microalgae characterized by their unique silica cell wall. Green algae are a group of photosynthetic eukaryotes present in a variety of environments (marine environments, continental freshwater, and brackish water wetland habitats). These groups are very diverse today, but they are also very diverse in the fossil record.

Sedimentary structures

The choice of mat cracks is based on field observations. For the modern register, we investigated the ponds of Bages and Thau in France at the beginning of 2024. We could observe modern mat cracks developing in natural environments and to note the variability of the structures present according to variations in wet and dry environmental conditions and to micro-organism consortium types. Furthermore, in the Montagne Noire region near the Salagou lake, France, fossil mat cracks are present in rocks dating from the Permian period, where the formation of tears can clearly be identified.

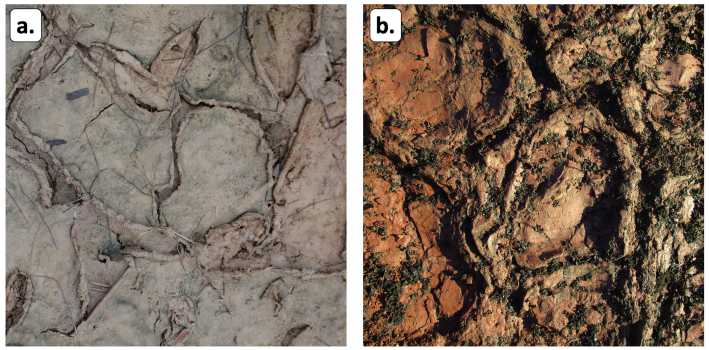

Different MISS records a. modern mat cracks observed at the ponds of Peyriac-de-Mer (France), c. fossil mat cracks observed at the Montagne Noire near the Salagou lake (France)

MATERIAL & METHODS

Digital elevation models, orthophotos and geomorphometric derivatives production

Dense point clouds, 3D models, digital elevation models (DEM) and orthophotos were computed using the standard workflow of the Metashape photogrammetric software applied to the 21 context-images of each tray (Rose et al., 2022). Scaling of the photogrammetric products was done using height referenced markers, identically arranged around all the tray edges, in a submillimetric grid accuracy. The root mean square error (RMSE) of the scaling operation ranges from 0.2 to 0.7 mm. Then, a systematic clipping was performed to remove the plastic edges of the trays from the 3D scenes. Therefore, all photogrammetric products are superimposable and can be robustly compared from each other to assess morphometric variation among treatments with a submillimetric accuracy. Dense point clouds range from 3 to 7.5 million points. DEM resolution ranges from 0.11 to 0.15 mm whereas orthophotos resolution ranges from 0.06 to 0.08 mm. For convenience, all orthophotos were resampled to 0.08 mm in resolution.

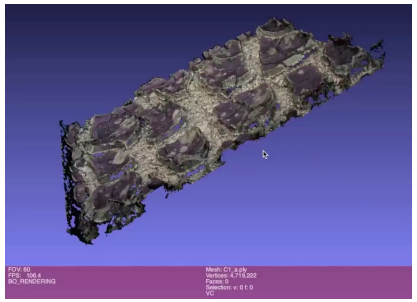

Video of the C1a treatment's dense points cloud

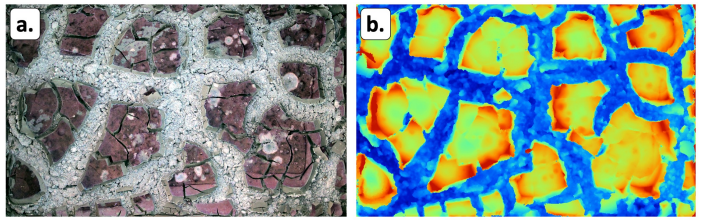

C1a treatment:
a. Orthophoto,
b. Digital Elevation Model

Digital elevation models (DEMs)

From each of the 50 DEMs, eight typical geomorphometric rasters (Hengl and Reuter, 2008) were derived in order to quantitatively capture the topographical and morphological arrangements emerging from the experiment: Slope, Aspect, Curvature, Sky View Factor (SVF), Multi-Scale Topographic Position Index (TPI), Terrain Ruggedness Index (TRI), Vector Ruggedness Measure (VRM) and the so-called geomorphons derivatives were computed from the DEM using RSAGA algorithms (Brenning, 2008; Conrad et al., 2015).

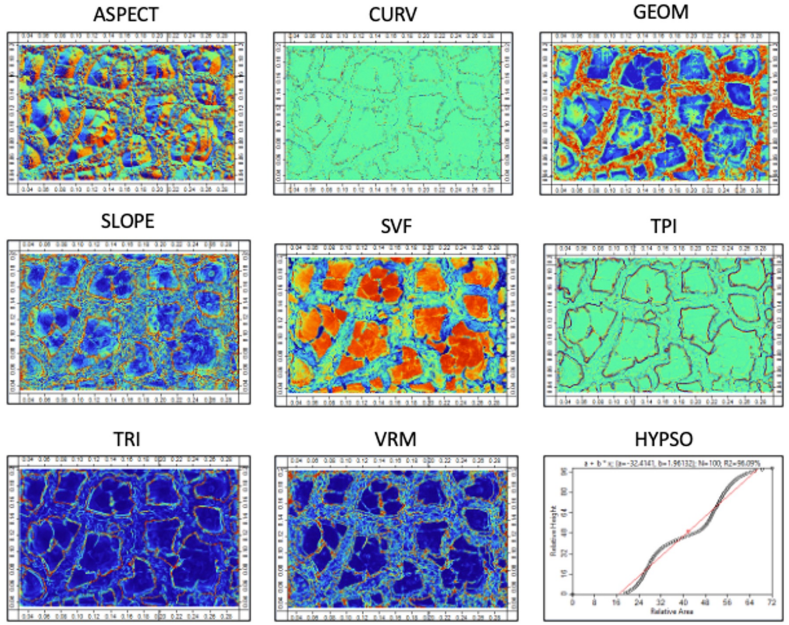

Geomorphometric rasters of the C1a treatments: Aspect, curvature (CURV), geomorphon (GEOM), slope, sky view factor (SVF), multi-scale topographic position index (TPI), terrain ruggedness (TRI), vector ruggedness measure (VRM), and hypsometric curves (HYPSO)

MATERIAL & METHODS

Digital elevation models (DEMs)

Aspect, Curvature, and Slope: the most widely used topographic metrics and were computed following the method of (Zevenbergen and Thorne, 1987).

Geomorphon: raster dataset that classifies DEM into ten types of terrain forms (flat, summit, ridge, shoulder, spur, slope, depression, valley, footslope, hollow) based on local topography analysis through line-of-sight principle in 8 different directions (Jasiewicz and Stepinski, 2013). The geomorphon rasters were calculated using a radial limit of line-of-sight computation of 30 cm (i.e., equivalent to the length of the widest edge of the tray) and a flatness threshold angle (angle below which the pixel is classified as flat) of 1 degree.

Hypsometric curves: compare the distribution of elevations between treatments and biomass levels and expressed the proportion of area above relative height (Strahler, 1964; Willgoose and Hancock, 1998).

Multi-Scale Topographic Position Index (TPI): calculated by averaging the DEM over a user-defined moving window size (expressed as a radius in pixel) and subtracting the original DEM from the averaged version to get the residual (Guisan et al., 1999). TPI extracts finer-scale landforms from regional-scale relief (Positive TPI values represent ridges or hills, and negative TPI values represent valleys or pits). The multiscale version of TPI calculates a standardized TPI over multiple neighbourhood radii from 1 to 8 pixels wide, starting at the largest neighbourhood size. For subsequent steps, the standardized TPI is updated with pixels where the absolute TPI values exceed the TPI values of the previous step.

Sky View Factor (SVF): gives the portion of visible sky, limited by the surrounding relief, from each cell. It is computed with a search radius of 30 cm (i.e., equivalent to the length of the widest edge of the tray) using the method of (Zakšek et al., 2011).

Terrain Ruggedness Index (TRI): represents the mean change in elevation between a grid cell and its neighbours, over a moving window of 5 pixels radius (Riley et al., 1999).

Vector Ruggedness Measure (VRM): calculated by decomposing slope and aspect into 3-dimensional vectors and calculating the resultant vector magnitude within a moving window of 5 pixels radius (Sappington et al., 2007).

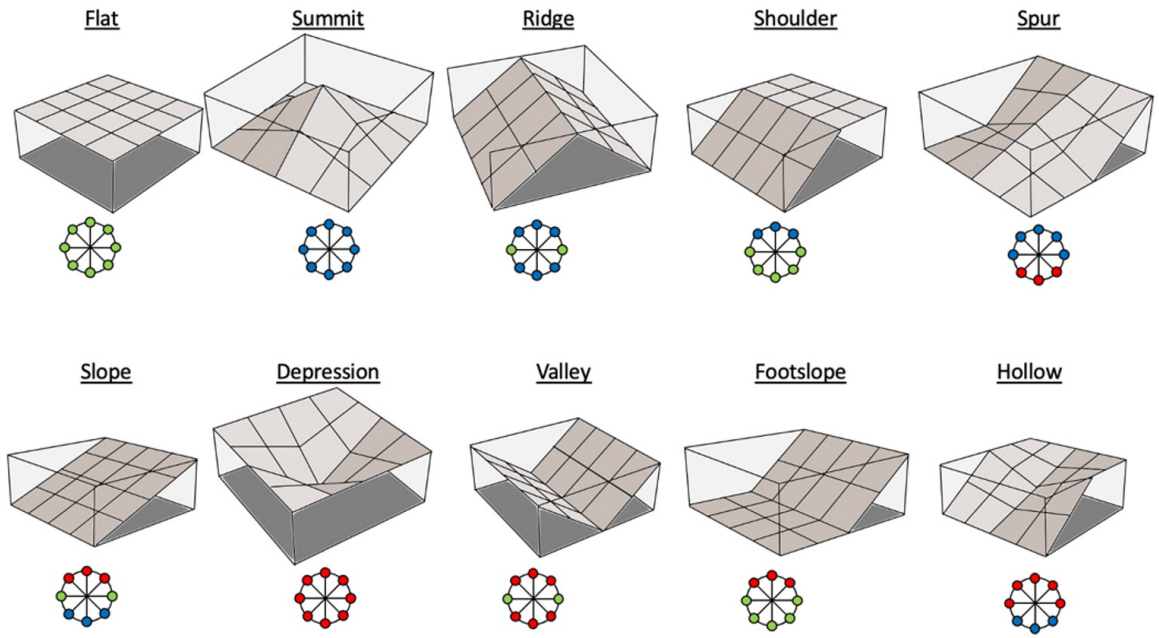

Different geomorphons

Data compilation and exploration

The Kruskal-Wallis test (one-way analysis of variance) was used to study the variability of treatments (A, C, D, G, and M) and biomasses (1 and 2) between them, but also as a function of the different geomorphons.

Summary statistics for each geomorphometric rasters and for each tray were computed and assembled in a data frame for multivariate data exploration using Principal Component Analysis (PCA) and Hierarchical Clustering on Principle Components (HCPC) using the R FactoMineR package.

MATERIAL & METHODS

Automated image slicing and DEM derivatives for AI

This method consists of slicing the initial image into 512x512 pixel tiles to be adapted for AI processing. The algorithm reads the original image, determines its size, calculates the number of overlap pixels to be applied and slices the image. The idea is then to apply the same slicing to the DEM and its derivatives.

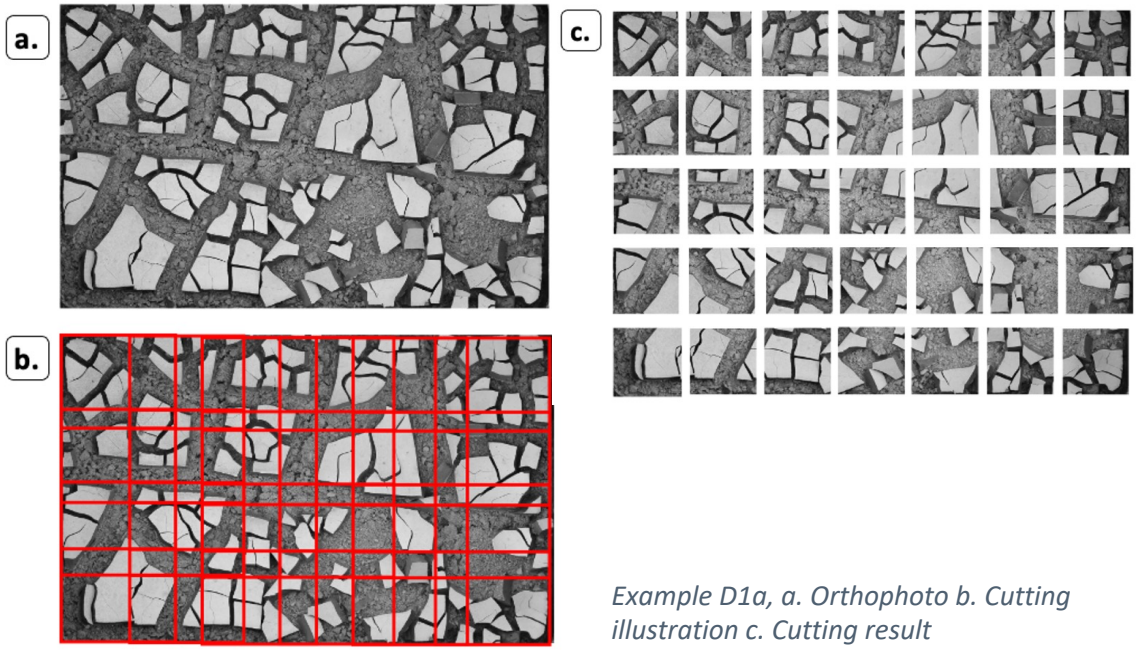

Example D1a, a. Orthophoto b. Cutting illustration c. Cutting result

The first difficulty is that, although these metrics can be represented in image form, they are not images, because the format of each pixel is either a real or an integer, but not a step in the range. The solution is to use the Tiff format, which allows images to be stored with a variable number of layers (which can go beyond 3, such as R, G, B) and, above all, to store something other than integer values between 0 and 255.

Another problem concerns the format of DEM derivatives compared with the initial image: the resolution, the number of pixels, is not the same, the resolution being higher for orthophoto than for DEM and derivatives. In addition, the resolution of the orthophoto is not a multiple of that of the derivatives. To reconstitute the DEM derivatives with the same resolution as the orthophotos and given that we don't periodically come back to the initial values, we interpolated all the points. This is what was programmed, and once the derivatives had been interpolated, they were automatically cut so that they could be superimposed on the sub-images derived from the orthophoto.

A total of 35 sub-images were obtained for each tank image. There are 50 tanks, making a total of 1,750 sub-images of 512 x 512 pixels to be analyzed by the CNN.

CNN procedure

The set of images was divided into three subsets: a learning/validation set representing 80% (1400 images), of which 75% and 25% were respectively dedicated for learning and validation phases. The remaining 20% (350 images) testing set was designed so that each modality (C1, C2, D1, D2, G1, G2, M1, M2, and A) was represented by pictures extracted from a tray that had never been used during the training/validation phase.

As the dataset size was not sufficient to train a CNN from scratch, a transfer learning approach was adopted using a Resnet50 pre-trained on ImageNet. Resnet CNNs have proven their high capacities to deal with a wide variety of cases (classification, detection, and localization). ResNet50 is a good compromise between the performances and the computational needs (He et al., 2016). The training was done on the classification layer while freezing the deepest layers. Cross-Entropy Loss as loss function and Adam optimizer with a

MATERIAL & METHODS

learning rate of 0.001 and a weight decay of 0.0001 were used to train the model. The training was done on 20 epochs with batches of 64 images. Several data augmentation methods (i.e., Augmix (Hendrycks et al., 2020), RandAugment (Cubuk et al., 2020), TrivialAugment (Müller and Hutter, 2021)) were tested but did not improve the generalization ability of the model, most likely due to the well-controlled picture acquisition.

To explore features that drive the model decision, two visualization methods were chosen: Grad-CAM++ (Chattopadhay et al., 2018) and FullGrad-CAM (Srinivas and Fleuret, 2019). Thus, Guided Grad-CAM++ and Guided-FullGrad-CAM were implemented, consisting in a combination of ReLU backpropagation with respect to DeconvNets (Zeiler and Fergus, 2014).

Model performances were evaluated in terms of global accuracy computed on the summed errors of each class to predict.

RESULTS & DISCUSSION

Ex situ observations

From the dried results of experiments carried out at the CRBE laboratory in Toulouse, we have obtained mat cracks.

Observation levels

There are a first sandy topographic level (bottom) and a second clay topographic level (top) with (C, D, G and M) or without (A) the presence of a biofilm on the latter. A network of primary cracks is observed, corresponding to the widest separations between the clay parts, where the sandy matrix below can be seen. Networks of secondary cracks are visible on the sandy (parallel to the primary cracks) and clayey (not parallel to the primary cracks) levels.

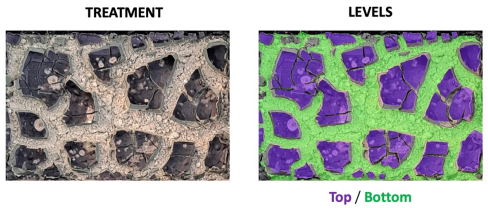

Example C1a: two distinct topographic levels

These different levels of results are used to provide an overall description in three parts: texture, shape, and pattern of each bin. Texture corresponds to the arrangement of sand and clay grains (sand/clay ratio and cracks), and particular structures on biofilms (e.g., fungi, bubbles, filaments, detachment). Shape defines a clay level distinct from other clay levels within the same tray, apart from the primary cracking network, but including a network of secondary cracks. Pattern corresponds to the arrangement of the different shapes around the primary crack network.

We were able to observe variability in texture, shape, and pattern of the different strains among themselves (C, D, G and M) and with the abiotic control (A), but also between the different biomasses (1 and 2) whether in similar or different strains.

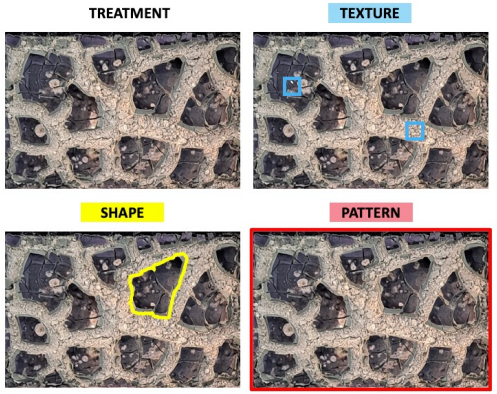

Example C1a: full processing, texture, shape, and pattern

RESULTS & DISCUSSION

Observed differences

Proportion between the sandy and clayey levels of a tank: A, G1 and D have a sandy level with a lower proportion than that of the low topographical level corresponding to the clayey part. Classes C, D and G have these two levels in equivalence. Shrinkage during the drying process is therefore less significant in A, G1 and D than in C, G2 and M.

Cracks: The primary network of cracks is thin in A, thin and thick in D and G1, and thick in C, G2 and M. The secondary network of cracks on the clay level is not very present in A, C, G2 and M, whereas it is in D and G1. A is affected regularly in both first order and second-order desiccations. For strains, where a treatment will be impacted by the primary crack network, it will be less affected by the secondary network, and vice versa.

Biofilms: A has no biofilms. All strains show fungal growth on their biofilms, which increases as biomass increases. C2, G2 and M2 show large filaments between the torn parts of the biofilms. C and M show biofilm detachment from the clay part. Strong biomasses are those with the most advanced biotic development on their biofilms, and detachment occurs on the two most concentrated treatments (C and M), so we can assume that the formation of marked biotic structures increases with increasing biotic concentration in the environment.

Shape types: A, D1 and G1 have angular clay shapes. C, D2 and G2 have angular and irregular clay shapes. M has irregular clay shapes. Desiccation may be disrupted by high biotic presence (M and C have the highest biomass 1 and 2 and D2 and G2 also show irregular shapes).

Size of shapes: A, C, G and M show slight variations in the size of their shapes, but these sizes remain roughly in the same range. Size differences are much more pronounced within the shapes of D. Desiccation could be non-homogeneous across the whole of a single tray in treatment D.

Colors: A is light gray. C and M have biomasses 1 and 2 that are dark brown and brown respectively. D1 is white and D2 is dark gray. G is green. C could be the source of M's color among the mixture of C, D and V that make up the latter.

Overview

Abiotic control A stands out from all the strains in that it has no biofilms and homogeneous shapes. Treatments C and M have similar characteristics (sand/clay ratio, desiccation, shape range, color). D is visually closer to A, with a more angular, clean-cut appearance, as in the abiotic control. G is a little closer to the C and M consensus, although G1 will tend slightly towards D (sand/clay ratio, desiccation, biofilms, shape range), while G2 is closer to C2 and M2 (sand/clay ratio, desiccation, shape range).

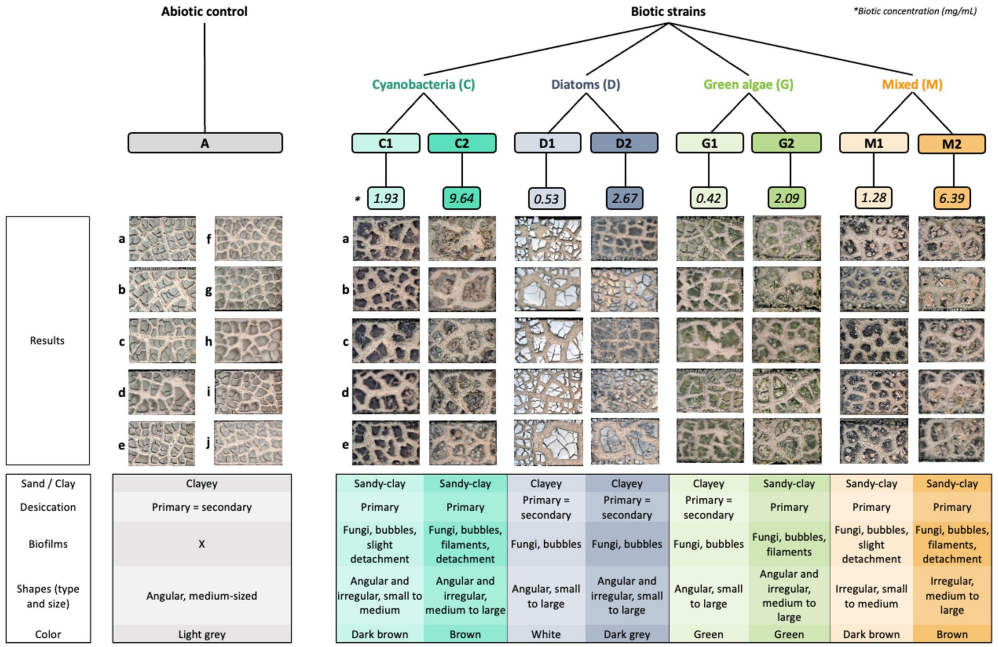

Pattern variations with the different treatments (A, C1, C2, D1, D2, G1, G2, M1, M2) with different biotic concentrations

RESULTS & DISCUSSION

Statistical analyses

Using various statistical tools, we sought to understand the variability observed within the different treatments of this experiment.

Continuous geomorphometric rasters

Kruskal-Wallis

No significant differences were observed for Aspect, Curvature and TPI. For DEM, significant differences are shown on the graph, indicating variability in the reliefs and morphologies of the different treatments A, C, D, G, and M. For Slope, there is a significant decrease in biofilm-induced slope values, especially for diatoms. The biotic treatments maintain a smoother topography, while the abiotic control has steeper slopes. The Sky view factor (SVF) is significantly higher for diatoms, as the relief of this class is concentrated higher up than that of the others (including abiotic control). Roughness (TRI & VRM) is significantly lower for diatoms.

PCA

We can see that SVF, Curvature, Slope and VRM are well represented on the graph, unlike Aspect, TPI and DEM. Aspect and Curvature are well correlated with each other, TPI with DEM, and Slope with VRM and TRI. SVF is independent of the other rasters and inversely correlated with the first axis. Aspect and Curvature are well represented by the second axis and poorly by the first, and vice versa for Slope, VRM and TRI. We can therefore deduce that the first axis corresponds to the slopes of the various reliefs and the second to the curvatures.

With the representation of individuals in classes A, C, D, G and M, we can begin to see trends emerging. Abiotic control is distinct from biotic treatments in the upper right of the graph. This class is correlated with the slopes of the different landforms. Classes C and M in particular, but also G, merge in the center of the graph. D is distinct from A and the other three biotic classes, and correlates more with SVF.

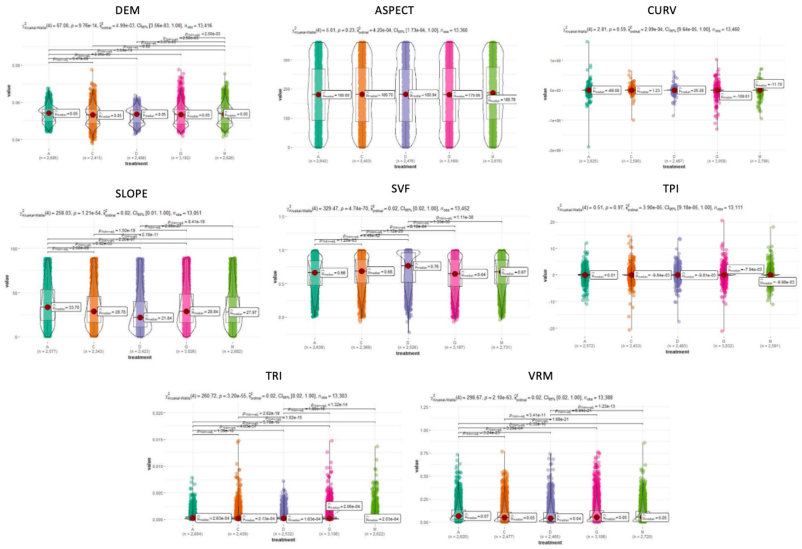

Graphs of Kruskal-Wallis tests, one-way ANOVA, for the different continuous geomorphometric rasters: Digital elevation model (DEM), Aspect, Curvature (CURV), Slope, Sky view factor (SVF), Multi-scale topographic position index (TPI), Terrain ruggedness (TRI), and Vector ruggedness measure (VRM)

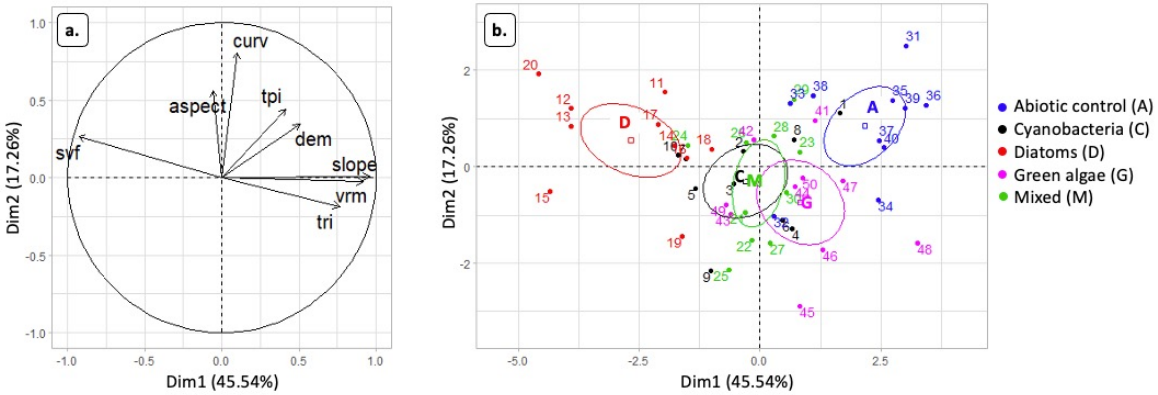

PCA: continuous geomorphometric rasters and A, C, D, G, and M classes

RESULTS & DISCUSSION

Geomorphons

Within the entire dataset, the geomorphons represented are depression, flat, hollow, ridge, slope, spur, peak, and valley. Flat, footslope and shoulder geomorphons are present at negligible levels.

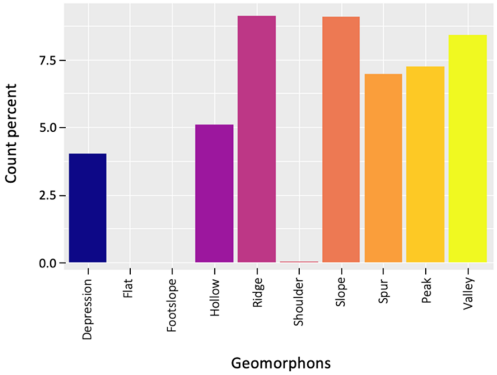

Count percent of geomorphons in the entire dataset

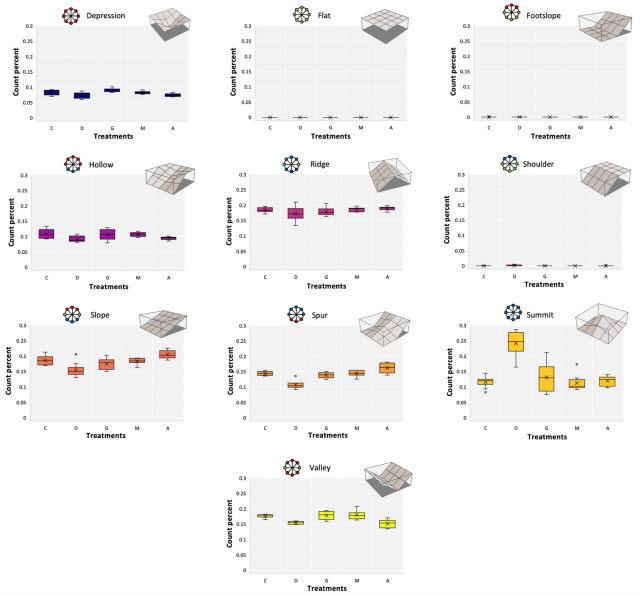

Boxplots of the geomorphons distribution in the different treatments

Treatments C, M and A don't show much intra-group variation for the different tanks. On the other hand, D and G have high intra-group variability for summit, which explains the extent of the boxplots seen above for this geomorphon.

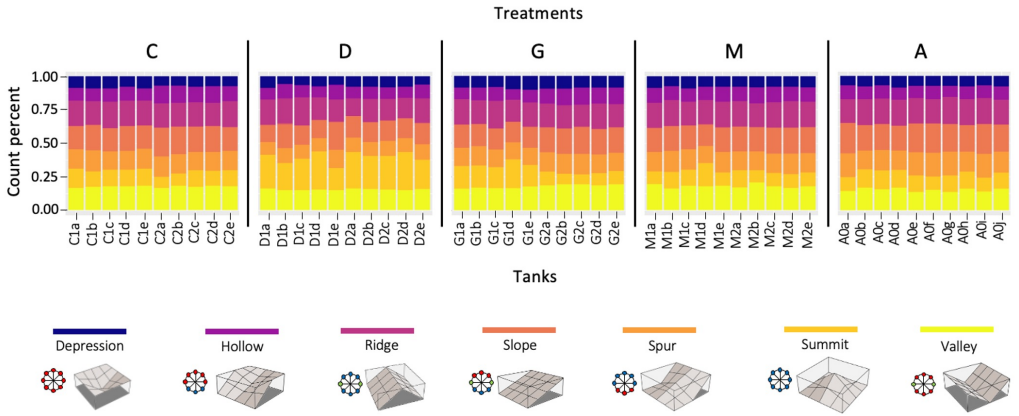

Variability of geomorphons between treatment tanks

Well-represented geomorphons vary according to different biomasses. At zero biomass, geomorphons are less pronounced. Between biomass 1 and 2, geomorphons depression and spur do not vary. As biomass 1 increases to 2, hollow, valley and slope increase, while ridge and peak decrease. For biomasses 0 and 2, slope is in the majority and for biomass 1, ridge is in the majority (and slope is not far off).

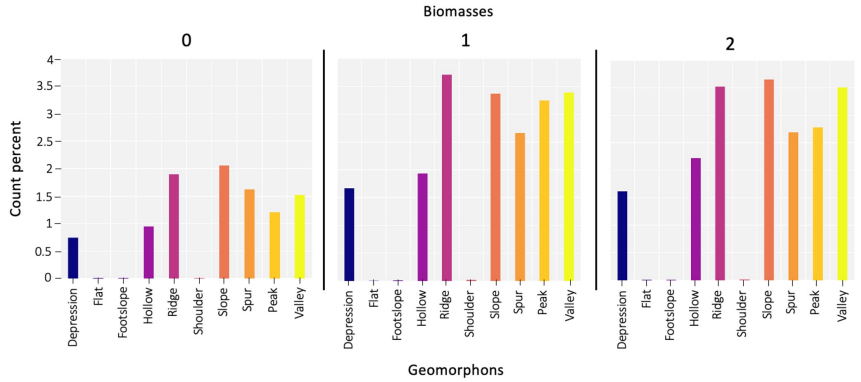

Representation of geomorphons as a function of biomass (0 = no biomass, 1 = low biomass, 2 = high biomass)

RESULTS & DISCUSSION

Topographic levels

From the hypsometric curves of DEM obtained for the different treatments, we can see that there is significant intra-group variance, whether for abiotic control (A), strain type (C, D, G and M) or biomass (1 and 2). We can therefore assume that there is a difference evaluated on an accentuated bimodality criterion, with a first modality at low altitude (areas where the sandy matrix can be seen) and a second modality at high altitude (upper clay plateaus with or without the presence of biofilms).

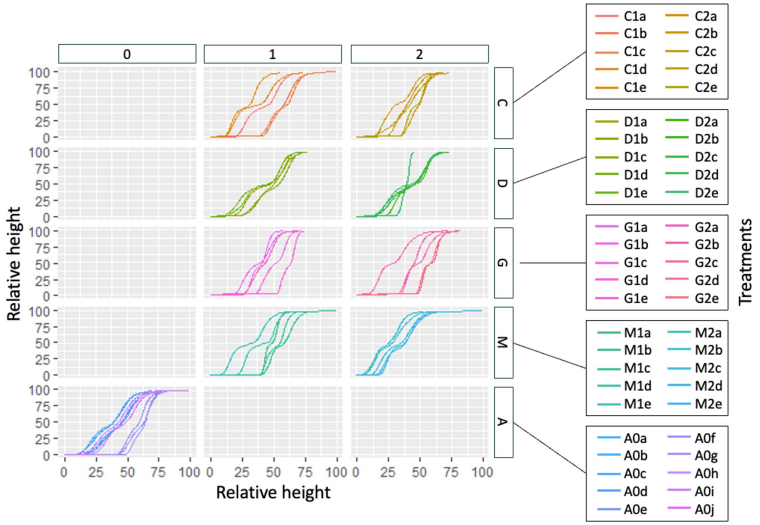

Hypsometric curves for the different treatments according to their strain type (or absence for A) and their different biomasses (except for A, which has a zero biomass by definition)

To better distinguish the variation of this bimodality between the different biotic strains, we compared the distribution of heights according to treatments by comparing the position of the modes (summit vs. valleys) to the abiotic reference.

For the biotic treatments, the "valley" modality increases in relation to the abiotic control. On the other hand, compared to the abiotic control, the "summit" modality decreases in the case of cyanobacteria (C), green algae (G) and mixed algae (M), and increases in the case of diatoms (D).

C and G have similar variations, which induce an equivalence in the flat/valley distribution. D has a variation that accentuates the abiotic trend, increasing the representation and the flat/valley distinction. M reverses the trend of the abiotic control: for the abiotic control, the "summit" modality is more important than the "valley" modality, and the opposite is true in the case of M.

In the 4 strain types, the flat/valley distribution is more differentiated.

These variations make it possible to distinguish three types of modification of abiotic control by biotic strains: equivalence of relief (C and G), increase in relief (D) and inversion of relief distribution (M). The presence of biotic strains will increase the contrast between the distribution of different reliefs.

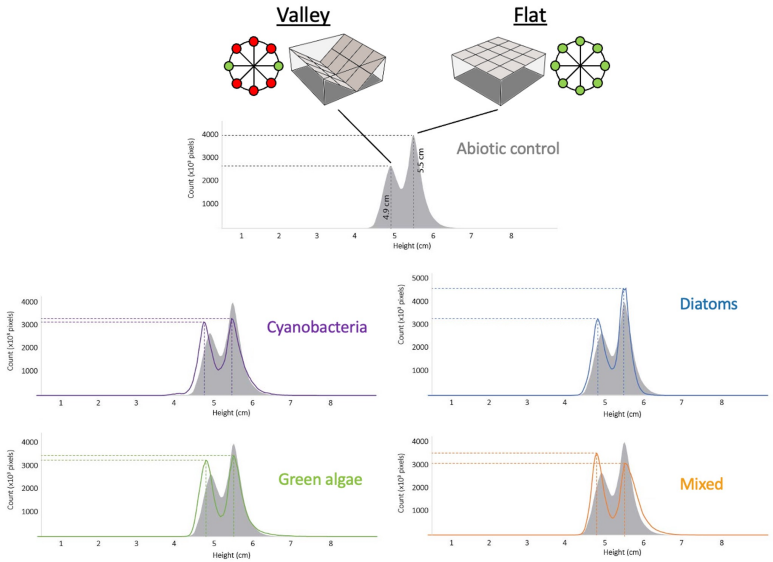

Height distribution by treatment (flats vs. valleys)

RESULTS & DISCUSSION

Color

The three components R, G, B (R: red, G: green, B: blue) of the orthophotos are very close to each other, resulting in the absence of a dominant color. Color is therefore not a discriminating criterion between treatments of the experiments.

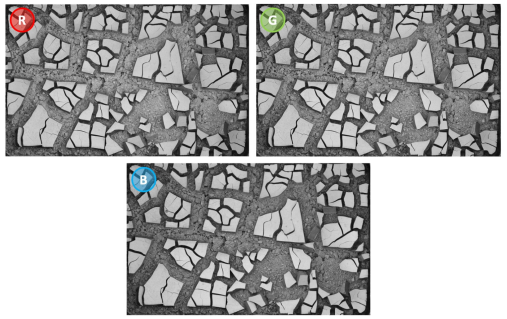

Example of D1a processing with R, G, B orthophoto components

CNN results

Initial classification results obtained by CNN show correct predictions of between 85% and 99%.

To visualize the neural network output of the 1750 sub-images, we use confusion matrices indicating the classifications made by the AI of the 9 different classes under study: A, C1, C2, D1, D2, G1, G2, M1, and M2. The rows of the matrix, labelled "Actual", correspond to the actual classes, and the columns of the matrix, labelled "Predictions", correspond to the AI's choice of classes.

For biotic strains (C, D, G, M) with different biomasses (1 and 2), we have multiplied the experiments 5 times, corresponding to batches a, b, c, d and e. The abiotic controls (A) were repeated 10 times (a, b, c, d, e, f, g, h, i and j), as they do not have different biomasses. It is then possible to look at the batches of strains separately in confusion matrices, including two abiotic control batches for each, making 350 sub-images to analyze. These different sets are then merged to produce a confusion matrix with 1750 sub-images.

Different treatments

Between the different versions, prediction confusion is between 10 and 15%, or 12.5% for all versions combined. It should be noted that some confusion occurs with A and different classes, especially G1. For biotic strains, confusions are mainly observed for C2, confused with G2, M1 and M2. Classes G1 and G2 are also confused with each other. Classes C1 and D1 are not much confused, except with their respective high biomass versions (C2 and D2). Class D2 is confused with D1, but also mainly with C2 and G1. Mixed (M) can be confused with other classes but are well distinguished between their weak biomass (1) and their strong biomass (2).

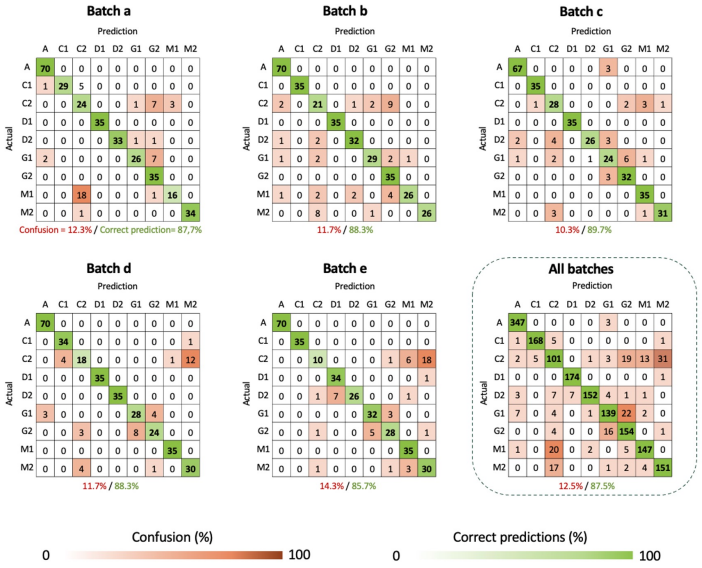

Confusion matrices for the different batches a, b, c, d, e, and the 5 batches together

The neural networks are 87.5% correct in their predictions between the different types of treatment (A, C1, C2, D1, D2, G1, G2, M1, M2), which is very encouraging. On the other hand, some classes were more difficult to define than others, such as C2 (101 correct predictions out of 175 images). The distinct strains (C, D and G) saw their low biomass (C1, D1 and G1) mostly confused with their high biomass (C2, D2 and G2), whereas the latter had more disparate confusions with the other classes. Mixed strains (M) may be confused with each other, but especially with class C2.

RESULTS & DISCUSSION

Different characteristics

From the confusion matrices, we can then isolate the characteristics (biomasses, strain types, biogenicity) for better visualization.

Similar biomasses and abiotic control: for low biomasses between them, confusion is almost zero (0.9%) and is mainly concentrated on G1 with A. For high biomasses between them, confusion is higher (8%) and is mainly concentrated on C2 and M2 (also a little G2 where C2 is confused with). This raises the question of whether increasing biomass tends towards a clear and similar distinction of biotic substrate for the different strains.

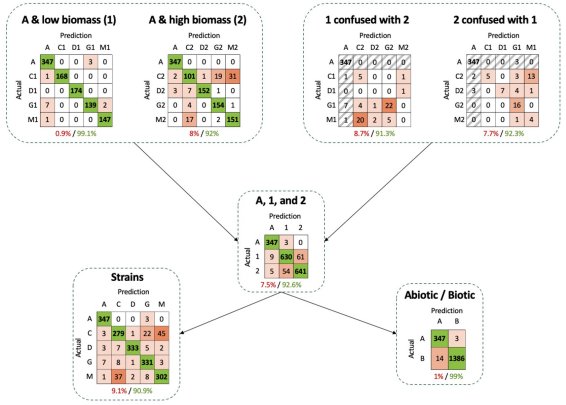

Visualization of confusion matrices as a function of biomass, strain type and biogenicity

Different biomasses: Low biomass is 8.7% confused with high biomass. Strong biomasses are confused at 7.7% with weak biomasses, which is equivalent to the reverse. Biomass confusions are mainly located (in both directions) on G1 with G2 and M1 with C2.

All biomasses and abiotic control: Confusion between the two different biomasses and their absence in the abiotic control is 7.5% and is mainly located between 1 with 2 and 2 with 1, which remain equivalent.

Different strain types and abiotic control: Between A, C, D, G, and M, the confusion is 9.1%. This confusion is mainly concentrated on C and M in both directions. We can therefore ask whether, within M, cyanobacteria (C) will exert a greater influence than diatoms (D) and green algae (G) in shaping the biogeomorphological structure and/or whether C had a selective advantage when growing M in the phytotron. Note that in M, C accounts for 62.8% of dry mass, while D and G represent 20.9% and 16.3% of dry mass respectively. Also, C is often classified in G, while G is less confused with C. We can therefore ask whether some types of strains (C, D and G) are closer than others. From the matrices here, we can assume that C and G are closer in terms of induced sedimentary structures than D.

Abiotic and biotic: Confusion between abiotic control and biotic treatments combined is 1%, which is very encouraging for this rock biosignature detection project.

Class Activation Maps (CAMs)

The various CAMs help us to understand how the image was classified by the CNN. Their analysis will enable us to understand, on a case-by-case basis, which zone of interest was used to classify the image. From the orthophoto sub-image, pixels will be activated to a greater or lesser extent. This activation can be visualized in the FullGrad-CAM section, with the most activated pixels in red and the least activated in blue. Note that red is not synonymous with a zone of interest, but rather with the area that has been analyzed the most. Guided Back Propagation-CAM and Guided-FullGrad-CAM show highly iridescent zones, which correspond to areas of interest. It's in Guided-FullGrad-CAM where the filter is the strongest, with few parts of the sub-image remaining. Areas of interest are highly iridescent, and relief can even be retraced.

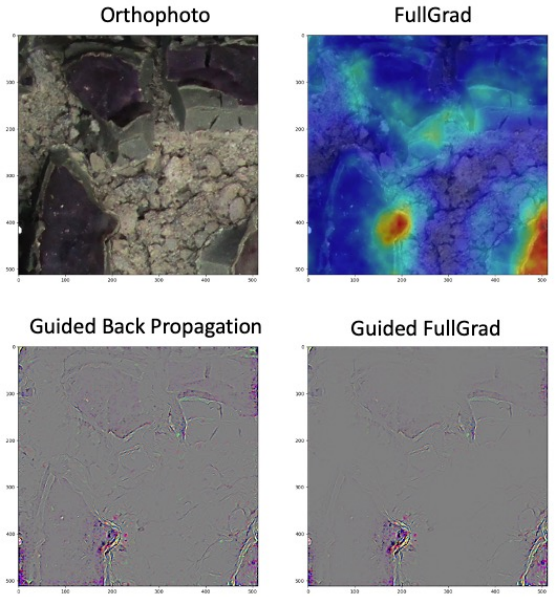

Orthophoto and Class Activation Maps (C1e sub-image 1)

CONCLUSION & PERSPECTIVES

Under controlled conditions, the laboratory experiment highlighted the variability between abiotic and biotic treatments, as well as within biotic treatments themselves, with or without different biomass scales. These initial observations showed that diatoms can be distinguished from other biotic treatments. What's more, the geomorphological modifications induced by the presence of biofilms are clearly visible to the naked eye when comparing abiotic controls.

Statistical analysis revealed trends in inter- and intra-group variability. Abiotic structures were clearly different, confirming initial observations. Diatoms again showed different relief trends, with plateaus being very present and reliefs less so, in contrast to the other treatments. PCA and distribution analyses showed a strong correlation between C and M. G is the class with the greatest intragroup variability, where G with low biomass will approach the characteristics of D, while G with high biomass will approach the characteristics of C and M. The presence of biomass causes landforms to vary in comparison with an abiotic control. As biomass increases, the hollows and slopes become more pronounced. These trends are reflected in the first outputs from neural networks.

The prediction results of CNN are very encouraging, showing a success rate of between 85% and 99%. Only 1% of abiotic structures are confused with biotic structures. Confusion is mainly observed between biotic classes. The classes with the greatest increase in confusion are between high biomass and C with M. C and M have higher basic concentrations than treatments D and G for both low and high biomass.

(i) Observations can be correlated on several scales: primary observations, statistical studies, deep learning.

(ii) Different or similar morphological trends can be highlighted using statistical tools and neural networks.

(iii) An increase in biomass can accentuate a trend towards convergence or morphological distinction, which can lead to confusion when classifying images.

To continue…

Success in distinguishing variability in abiotic and biotic structures under controlled laboratory conditions has prompted us to extend the field study to the ponds of Bages and Thau for the recent record, and to the Montagne Noire for the fossil record. These expeditions will provide a lot of data for AI and we will also add sedimentary and biofilms samples to do geochemical analysis.

Nevertheless, the development of new laboratory experiments will be necessary to explore new variabilities or deepen some already seen by increasing biomass (or reducing it) or varying the types of microorganisms and sediments used.

Large confusions are shown between C and M, and a CAM analysis is underway to try to understand which zones of interest are considered and whether they correlate with the statistical analyses.

Finally, the clear distinction between abiotic and biotic structures, as well as the possibility of intra-group classification (e.g., here between biotic treatments and/or biomass) are encouraging for the possible application of this study to the Martian question. Reflections on research angles and the application of the terrestrial protocol to Martian issues are underway.

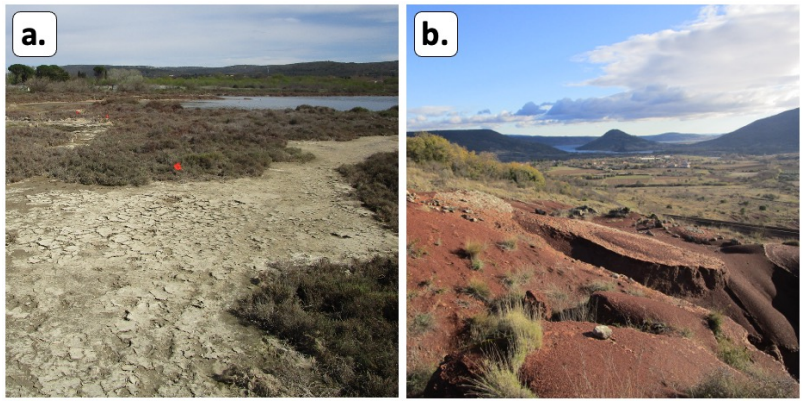

Fields, a. Pond of Thau (South of France), b. Salagou Lake (Montagne Noire, South of France)

ACKNOWLEDGMENTS

Collaborations & Partnerships

This work is a collaboration between several universities: the Université de Clermont Auvergne (Clermont-Ferrand, France), the Université Toulouse III - Paul Sabatier (Toulouse, France) and the University of Cambridge (Cambridge, UK). This research work is carried out in several French laboratories: Laboratoire de Géographie Physique et Environnementale (GEOLAB, UMR 6042, Clermont-Ferrand), Centre de Recherche sur la Biodiversité et l'Environnement (CRBE, UMR 5300, Toulouse) and the Geosciences Environnement Toulouse laboratory (GET, UMR 5563, Toulouse). AI development is in collaboration with MAD-Environnement (Nailloux, France).

Participation in AbSciCon2024 was made possible thanks to funding from GEOLAB, the Université de Clermont Auvergne and the Groupe Français de Géomorphologie, whom we thank.

AbSciCon2024

We would also like to thank the American Geophysical Union for giving us the opportunity to take part in AbSciCon2024, and Kimberly Warren-Rhodes who was the first to contact us and encourage us to come and present our research.

REFERENCES

Awramik, S.M., 2006. Respect for stromatolites. Nature 441, 700–701. https://doi.org/10.1038/441700a

Awramik, S.M., Grey, K., 2005. Stromatolites: biogenicity, biosignatures, and bioconfusion, in: Astrobiology and Planetary Missions. Presented at the Astrobiology and Planetary Missions, SPIE, pp. 227–235. https://doi.org/10.1117/12.625556

Bose, S., Chafetz, H.S., 2009. Topographic control on distribution of modern microbially induced sedimentary structures (MISS): A case study from Texas coast. Sedimentary Geology 213, 136–149. https://doi.org/10.1016/j.sedgeo.2008.11.009

Brenning, A., 2008. Statistical geocomputing combining R and SAGA: The example of landslide susceptibility analysis with generalized additive models. Hamburger Beiträge zur Physischen Geographie und Landschaftsökologie 19, 410.

Cady, S.L., Farmer, J.D., Grotzinger, J.P., Schopf, J.W., Steele, A., 2003. Morphological Biosignatures and the Search for Life on Mars. Astrobiology 3, 351–368. https://doi.org/10.1089/153110703769016442

Chattopadhay, A., Sarkar, A., Howlader, P., Balasubramanian, V.N., 2018. Grad-CAM++: Generalized Gradient-Based Visual Explanations for Deep Convolutional Networks, in: 2018 IEEE Winter Conference on Applications of Computer Vision (WACV). Presented at the 2018 IEEE Winter Conference on Applications of Computer Vision (WACV), pp. 839–847. https://doi.org/10.1109/WACV.2018.00097

Cohen, K.M., Finney, S.C., Gibbard, P.L., Fan, J.-X., 2013. The ICS International Chronostratigraphic Chart.

Conrad, O., Bechtel, B., Bock, M., Dietrich, H., Fischer, E., Gerlitz, L., Wehberg, J., Wichmann, V., Böhner, J., 2015. System for Automated Geoscientific Analyses (SAGA) v. 2.1.4. Geoscientific Model Development 8, 1991–2007. https://doi.org/10.5194/gmd-8-1991-2015

Corenblit, D., Darrozes, J., Julien, F., Otto, T., Roussel, E., Steiger, J., Viles, H., 2019. The Search for a Signature of Life on Mars: A Biogeomorphological Approach. Astrobiology 19, 1279–1291. https://doi.org/10.1089/ast.2018.1969

Corenblit, D., Decaux, O., Delmotte, S., Toumazet, J.-P., Arrignon, F., André, M.-F., Darrozes, J., Davies, N.S., Julien, F., Otto, T., Ramillien, G., Roussel, E., Steiger, J., Viles, H., 2023. Signatures of Life Detected in Images of Rocks Using Neural Network Analysis Demonstrate New Potential for Searching for Biosignatures on the Surface of Mars. Astrobiology 23, 308–326. https://doi.org/10.1089/ast.2022.0034

Cubuk, E.D., Zoph, B., Shlens, J., Le, Q.V., 2020. Randaugment: Practical Automated Data Augmentation With a Reduced Search Space. Presented at the Proceedings of the IEEE/CVF Conference on Computer Vision and Pattern Recognition Workshops, pp. 702–703.

Davies, N.S., Liu, A.G., Gibling, M.R., Miller, R.F., 2016. Resolving MISS conceptions and misconceptions: A geological approach to sedimentary surface textures generated by microbial and abiotic processes. Earth-Science Reviews 154, 210–246. https://doi.org/10.1016/j.earscirev.2016.01.005

Davies, N.S., Shillito, A.P., McMahon, W.J., 2017. Short-term evolution of primary sedimentary surface textures (microbial, abiotic, ichnological) on a dry stream bed: modern observations and ancient implications. PALAIOS 32, 125–134. https://doi.org/10.2110/palo.2016.064

Gerdes, G., 2007. Structures left by modern microbial mats in their host sediments, in: Atlas of Microbial Mat Features Preserved within the Clastic Rock Record. Elsevier, 1, pp. 5–38.

Gerdes, G., Krumbein, W.E., Noffke, N., 2000. Evaporite Microbial Sediments, in: Riding, R.E., Awramik, S.M. (Eds.), Microbial Sediments. Springer, Berlin, Heidelberg, pp. 196–208. https://doi.org/10.1007/978-3-662-04036-2_22

Greaves, J.S., Richards, A.M.S., Bains, W., Rimmer, P.B., Clements, D.L., Seager, S., Petkowski, J.J., Sousa-Silva, C., Ranjan, S., Fraser, H.J., 2021. Re-analysis of Phosphine in Venus' Clouds. Nat Astron 5, 636–639. https://doi.org/10.1038/s41550-021-01424-x

Guisan, A., Weiss, S.B., Weiss, A.D., 1999. GLM versus CCA spatial modeling of plant species distribution. Plant Ecology 143, 107–122. https://doi.org/10.1023/A:1009841519580

He, K., Zhang, X., Ren, S., Sun, J., 2016. Deep Residual Learning for Image Recognition. Presented at the Proceedings of the IEEE Conference on Computer Vision and Pattern Recognition, pp. 770–778.

Hendrycks, D., Mu, N., Cubuk, E.D., Zoph, B., Gilmer, J., Lakshminarayanan, B., 2020. AugMix: A Simple Data Processing Method to Improve Robustness and Uncertainty. https://doi.org/10.48550/arXiv.1912.02781

REFERENCES

Hengl, T., Reuter, H.I., 2008. Geomorphometry: Concepts, Software, Applications. Newnes.

Hofmann, H.J., Grey, K., Hickman, A.H., Thorpe, R.I., 1999. Origin of 3.45 Ga coniform stromatolites in Warrawoona Group, Western Australia. GSA Bulletin 111, 1256–1262. https://doi.org/10.1130/0016-7606(1999)111<1256:OOGCSI>2.3.CO;2

Jasiewicz, J., Stepinski, T.F., 2013. Geomorphons — a pattern recognition approach to classification and mapping of landforms. Geomorphology 182, 147–156. https://doi.org/10.1016/j.geomorph.2012.11.005

Kite, E.S., 2019. Geologic Constraints on Early Mars Climate. Space Sci Rev 215, 10. https://doi.org/10.1007/s11214-018-0575-5

Lapôtre, M.G.A., Bishop, J.L., Ielpi, A., Lowe, D.R., Siebach, K.L., Sleep, N.H., Tikoo, S.M., 2022. Mars as a time machine to Precambrian Earth. Journal of the Geological Society 179, jgs2022-047. https://doi.org/10.1144/jgs2022-047

Müller, S.G., Hutter, F., 2021. TrivialAugment: Tuning-Free Yet State-of-the-Art Data Augmentation. Presented at the Proceedings of the IEEE/CVF International Conference on Computer Vision, pp. 774–782.

Noffke, N., 2021. Microbially Induced Sedimentary Structures in Clastic Deposits: Implication for the Prospection for Fossil Life on Mars. Astrobiology 21, 866–892. https://doi.org/10.1089/ast.2021.0011

Noffke, N., 2015. Ancient Sedimentary Structures in the <3.7 Ga Gillespie Lake Member, Mars, That Resemble Macroscopic Morphology, Spatial Associations, and Temporal Succession in Terrestrial Microbialites. Astrobiology 15, 169–192. https://doi.org/10.1089/ast.2014.1218

Noffke, N., 2010. Geobiology: Microbial Mats in Sandy Deposits from the Archean Era to Today. Springer Science & Business Media.

Noffke, N., 2008. Turbulent Lifestyle: Microbial Mats on Earth's Sandy Beaches—Today and 3 Billion Years Ago. Geological Society of America Today 18. https://doi.org/10.1130/GSATG7A.1

Noffke, N., 1998. Multidirected ripple marks rising from biological and sedimentological processes in modern lower supratidal deposits (Mellum Island, southern North Sea). Geology 26, 879–882. https://doi.org/10.1130/0091-7613(1998)026<0879:MRMRFB>2.3.CO;2

Noffke, N., Awramik, S., 2013. Stromatolites and MISS—Differences Between Relatives. Geological Society of America Today 23. https://doi.org/10.1130/GSATG187A.1

Noffke, N., Beukes, N., Bower, D., Hazen, R.M., Swift, D.J.P., 2008. An actualistic perspective into Archean worlds – (cyano-)bacterially induced sedimentary structures in the siliciclastic Nhlazatse Section, 2.9 Ga Pongola Supergroup, South Africa. Geobiology 6, 5–20. https://doi.org/10.1111/j.1472-4669.2007.00118.x[22]

Noffke, N., Gerdes, G., Klenke, T., 2003. Benthic cyanobacteria and their influence on the sedimentary dynamics of peritidal depositional systems (siliciclastic, evaporitic salty, and evaporitic carbonatic). Earth-Science Reviews 62, 163–176. https://doi.org/10.1016/S0012-8252(02)00158-7

Noffke, N., Gerdes, G., Klenke, T., Krumbein, W., 1996. Microbially induced sedimentary structures-Example from modern sediments of siliciclastic tidal flats: Zeitbuch fur Geologie und Palaontologie, v. 1. Zeitbuch fur Geologie und Palaontologie.

Noffke, N., Gerdes, G., Klenke, T., Krumbein, W.E., 2001a. Microbially induced sedimentary structures indicating climatological, Hydrological and depositional conditions within recent and pleistocene coastal facies zones (Southern Tunisia). Facies 44, 23–30. https://doi.org/10.1007/BF02668164

Noffke, N., Gerdes, G., Klenke, T., Krumbein, W.E., 2001b. Microbially Induced Sedimentary Structures: A New Category within the Classification of Primary Sedimentary Structures. Journal of Sedimentary Research 71, 649–656. https://doi.org/10.1306/2DC4095D-0E47-11D7-8643000102C1865D

Pettijohn, F.J., Potter, P.E., 1964. Classification of primary sedimentary structures, in: Pettijohn, F.J., Potter, P.E. (Eds.), Atlas and Glossary of Primary Sedimentary Structures. Springer, Berlin, Heidelberg, pp. 3–9. https://doi.org/10.1007/978-3-642-94899-2_3

Pruss, S., Fraiser, M., Bottjer, D.J., 2004. Proliferation of Early Triassic wrinkle structures: Implications for environmental stress following the end-Permian mass extinction. Geology 32, 461–464. https://doi.org/10.1130/G2²0354.1

Rapin, W., Dromart, G., Clark, B.C., Schieber, J., Kite, E.S., Kah, L.C., Thompson, L.M., Gasnault, O., Lasue, J., Meslin, P.-Y., Gasda, P.J., Lanza, N.L., 2023. Sustained wet–dry cycling on early Mars. Nature 620, 299–302. https://doi.org/10.1038/s41586-023-06220-3

Riley, S.J., DeGloria, S.D., Elliot, R., 1999. A Terrain Ruggedness Index That Quantifies Topographic Heterogeneity. Intermountain Journal of Sciences 5.

Rose, W., Bedford, J., Howe, E., Tringham, S., 2022. Trialling an Accessible Non-Contact Photogrammetric Monitoring Technique to Detect 3D Change on Wall Paintings. Studies in Conservation 67, 545–555. https://doi.org/10.1080/00393630.2021.1937457

Sappington, J.M., Longshore, K.M., Thompson, D.B., 2007. Quantifying Landscape Ruggedness for Animal Habitat Analysis: A Case Study Using Bighorn Sheep in the Mojave Desert. The Journal of Wildlife Management 71, 1419–1426. https://doi.org/10.2193/2005-723

Schieber, J., Bose, P.K., Eriksson, P.G., Banerjee, S., Sarkar, S., Altermann, W., Catuneanu, O., 2007. Atlas of Microbial Mat Features Preserved within the Siliciclastic Rock Record. Elsevier.

Srinivas, S., Fleuret, F., 2019. Full-Gradient Representation for Neural Network Visualization, in: Advances in Neural Information Processing Systems. Curran Associates, Inc.

Strahler, A.N., 1964. Quantitative geomorphology of drainage basin and channel networks. Handbook of applied hydrology.

Viles, H.A., 2012. Microbial geomorphology: A neglected link between life and landscape. Geomorphology, Special Issue Zoogeomorphology and Ecosystem Engineering Proceedings of the 42nd Binghamton Symposium in Geomorphology, held 21-23 October 2011 157–158, 6–16. https://doi.org/10.1016/j.geomorph.2011.03.021

Westall, F., Foucher, F., Bost, N., Bertrand, M., Loizeau, D., Vago, J.L., Kminek, G., Gaboyer, F., Campbell, K.A., Bréhéret, J.-G., Gautret, P., Cockell, C.S., 2015. Biosignatures on Mars: What, Where, and How? Implications for the Search for Martian Life. Astrobiology 15, 998–1029. https://doi.org/10.1089/ast.2015.1374

Westall, F., Hickman-Lewis, K., Cavalazzi, B., Foucher, F., Clodoré, L., Vago, J.L., 2021. On biosignatures for Mars. International Journal of Astrobiology 20, 377–393. https://doi.org/10.1017/S1473550421000264

Willgoose, G., Hancock, G., 1998. Revisiting the hypsometric curve as an indicator of form and process in transport-limited catchment. Earth Surface Processes and Landforms 23, 611–623. https://doi.org/10.1002/(SICI)1096-9837(199807)23:7<611::AID-ESP872>3.0.CO;2-Y

Zakšek, K., Oštir, K., Kokalj, Ž., 2011. Sky-View Factor as a Relief Visualization Technique. Remote Sensing 3, 398–415. https://doi.org/10.3390/rs3020398

Zeiler, M.D., Fergus, R., 2014. Visualizing and Understanding Convolutional Networks, in: Fleet, D., Pajdla, T., Schiele, B., Tuytelaars, T. (Eds.), Computer Vision – ECCV 2014. Springer International Publishing, Cham, pp. 818–833. https://doi.org/10.1007/978-3-319-10590-1_53

Zevenbergen, L.W., Thorne, C.R., 1987. Quantitative analysis of land surface topography. Earth Surface Processes and Landforms 12, 47–56. https://doi.org/10.1002/esp.3290120107